Crustal structure of the northeastern Tibetan plateau, the Ordos block and the Sichuan basin from ambient noise tomography[*]

Yong Zheng [1,♣]   Yingjie Yang [1,2]   Michael H. Ritzwoller [2]
Xiufen Zheng [3]   Xiong Xiong [1]   and   Zuning Li [4]

[1] *Key Laboratory of Dynamic Geodesy, Institute of Geodesy and Geophysics,*
Chinese Academy of Sciences, Wuhan 430077, *China*

[2] *Department of Physics, University of Colorado, Boulder CO* 80303, *USA*

[3] *Institute of Geophysics, China Earthquake Administration, Beijing* 100081, *China*

[4] *Earthquake Administration of Fujian Province, Fuzhou* 350003, *China*

Abstract   We apply ambient noise tomography to significant seismic data resources in a region including the northeastern Tibetan plateau, the Ordos block and the Sichuan basin. The seismic data come from about 160 stations of the provincial broadband digital seismograph networks of China. Ambient noise cross-correlations are performed on the data recorded between 2007 and 2009 and high quality inter-station Rayleigh phase velocity dispersion curves are obtained between periods of 6 s to 35 s. Resulting Rayleigh wave phase velocity maps possess a lateral resolution between 100 km and 200 km. The phase velocities at short periods (<20 s) are lower in the Sichuan basin, the northwest segment of the Ordos block and the Weihe graben, and outline sedimentary deposits. At intermediate and long periods (>25 s), strong high velocity anomalies are observed within the Ordos block and the Sichuan basin and low phase velocities are imaged in the northeastern Tibetan plateau, reflecting the variation of crustal thickness from the Tibetan plateau to the neighboring regions in the east. Crustal and uppermost mantle shear wave velocities vary strongly between the Tibetan plateau, the Sichuan basin and the Ordos block. The Ordos block and the Sichuan basin are dominated by high shear wave velocities in the crust and uppermost mantle. There is a triangle-shaped low velocity zone located in the northeastern Tibetan plateau, whose width narrows towards the eastern margin of the plateau. No low velocity zone is apparent beneath the Qinling orogen, suggesting that mass may not be able to flow eastward through the boundary between the Ordos block and the Sichuan basin in the crust and uppermost mantle.

Key words: phase velocity; Ordos block; ambient noise tomography; crustal structure
CLC number: P315.2   **Document code**: A

1 Introduction

The collision of the Indian and Eurasian plates not only causes significant elevation of the Tibetan plateau, but also acts an important effect on remote areas such as the North China block to the east and the Baikal rift to the north (Molnar and Tapponnier, 1975; Tapponnier and Molnar, 1977; Bendick and Flesch, 2007). Because of the northward movement of Indian plate at a rate of ~5 cm/a, materials inside the Tibetan plateau are forced to escape towards the east. At the eastern boundary of the Tibetan plateau, the materials are blocked by the Sichuan basin and the Ordos block and are forced to change direction from eastward to northeastward and southeastward along a series of strike-slip fault systems. These faults include the Kunlun fault and the Xianshuihe-Zemuhe-Xiaojiang fault (e.g., Molnar and Tapponnier, 1975; Tapponnier and Molnar, 1977).

Although lateral extension and escape are apparent in the eastern part of the Tibetan plateau, some studies have demonstrated that lower crustal flow may be responsible for the high topography in the eastern plateau (Royden et al., 1997, 2008; Clark et al., 2005). During this process, strain accumulates slowly along the Long-

menshan fault zone, which then generated the 2008 May 12th Wenchuan earthquake (Burchfiel et al., 2008), for example. Lower crustal flow is assumed to split into two branches: one channel thought to flow to the south of Longmenshan fault and finally to the Yunnan region and the other is believed to flow northeast along the Qinling orogen between the Ordos and Sichuan blocks (Zhang et al., 1998; Huang et al., 2008). The status and mode of the crustal flow still remain unclear, however. Higher resolution 3D models of crustal and upper mantle structure would help to clarify these. If material flow does exist in the crust, the strength of the crust should vary vertically and laterally. Some researchers, such as Royden et al. (1997, 2008) and Clark et al. (2005), proposed that crustal flow in eastern Tibet is concentrated principally in the lower crust, while others hypothesized that lateral extrusion may be distributed widely within the asthenosphere (e.g., Huang et al., 2008).

During the past decades, scientists have performed a number of studies on crustal and lithospheric structure in the eastern Tibetan plateau and the Ordos block. For example, Liang and Song (2006) obtained a Pn tomographic image beneath the northern and eastern Tibetan plateau and found a low velocity belt extending from west to east beneath the Qiangtang block and the Songpan Garze fold belt in the northern Tibetan plateau. Huang et al. (2008) found shear wave splitting within the southern margin of the Ordos block and the directions of the fast S-wave subparallel to the trends of surface structures. However, because of limitations in the distribution of seismic networks and earthquakes, most of earlier studies mainly focused on the southwestern part of the Ordos block and few studies have been performed in the northeastern Tibetan plateau, the Qinling orogen and the interior and the eastern part of the Ordos block. Furthermore, seismic stations surrounding the study region in the past was quite sparse, which resulted in relatively low resolution of crustal and lithospheric structures. Fortunately, since the beginning of the Tenth Five-Year Project of China, there has been a growth in the number of broadband seismic stations deployed in the study region, which now provides higher quality of continuous seismic records to probe the crustal and mantle velocity structures at a much higher spatial resolution. Based on these data, we adopt the ambient noise tomography method (e.g., Shapiro et al., 2005; Moschetti et al., 2007; Bensen et al., 2008; Lin et al., 2008; Yang et al., 2008) to obtain a high resolution v_S model of the crust of the Ordos block and its surrounding areas.

2 Data processing

The data used in this study are continuous seismic waveforms recorded at broadband stations from the Chinese provincial digital seismograph networks from 2007 to 2009. The locations of stations are shown as triangles in Figure 1. In total, we process data from approximately 160 stations.
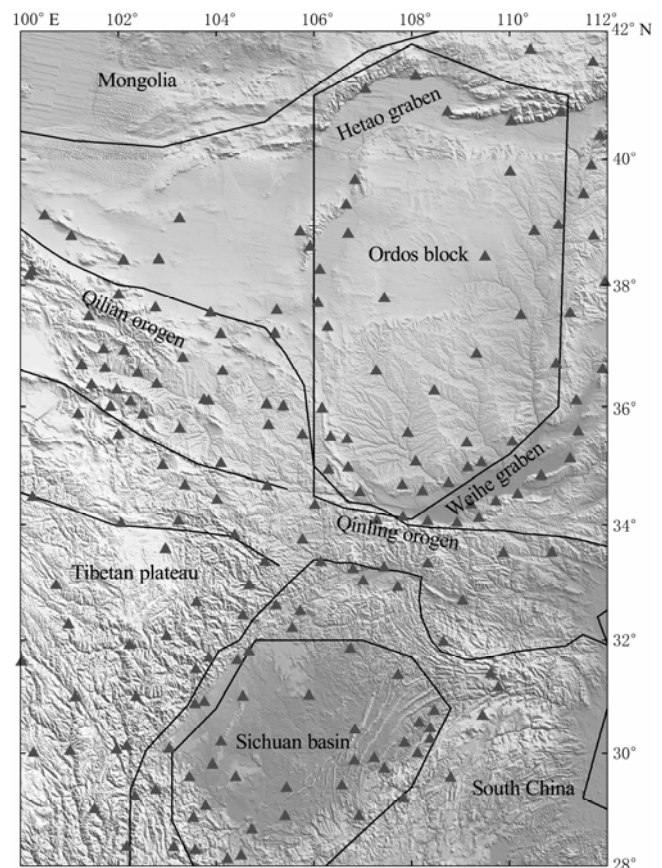

Figure 1 Tectonic units and the distribution of broadband seismic stations in the study region. The black lines outline the boundaries of different blocks and the triangles denote the locations of the seismic stations.

The data processing procedure applied here is similar to that defined by Bensen et al. (2007), and the one-bit method is used to remove the disturbances of earthquakes. In this work, only vertical components of ambient noise signals are analyzed. Thus, the cross-correlations contain only Rayleigh waves. We filter the data between 4 s and 50 s period. Figure 2 shows an example of cross-correlations between randomly selected stations. Both positive and negative correlation lags show clear surface waves with an average move-out velocity of ~3 km/s. The signals at positive and negative lags represent

waves travelling in opposite directions between each pair of stations and because they sample the same media they are expected to travel with the same dispersion characteristics. To enhance the SNR, we separate each cross-correlation into positive and negative lag components and then average the two components to form a final cross-correlation, which we call the "symmetric component". SNR is defined as the ratio of the peak am-

plitude within a time window containing the surface wave signals to the root-mean-square of the noise trailing the signal arrival window. The signal window was determined using the arrival times of Rayleigh waves at approximate minimum and maximum velocities of 2.5 and 4.5 km/s. The period dependence of the SNR was determined by applying a series of narrow band-pass filters centered on a grid of periods.
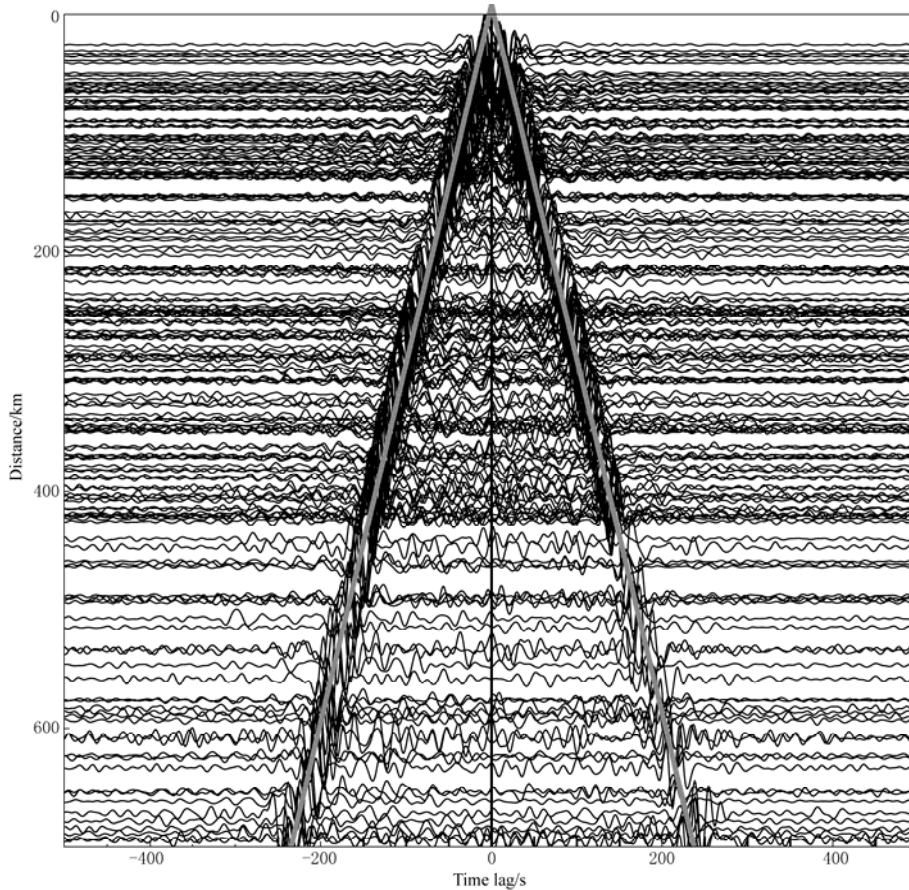

Figure 2 Record section of broadband (5−35 s period) cross-correlations from some randomly selected station pairs. Both positive and negative correlation lags appear in these cross-correlations. The two gray lines mark a moveout velocity of 3 km/s.

After we obtain all cross-correlations and calculate the signal-to-noise ratio (SNR), we apply two selection criteria prior to tomography. First, we accept measurements only when the distance between two stations is greater than three wavelengths. Second, we also use SNR to select acceptable measurements. At individual periods, only those measurements with SNR higher than 15 are accepted. After applying the criteria, we finally obtain between ~1 500 and ~11 000 phase speed measurements for tomography at periods ranging from 6 to 35 s (Figure 3). The number of measurements maximizes between periods of 10 and 20 s, i.e., in the primary
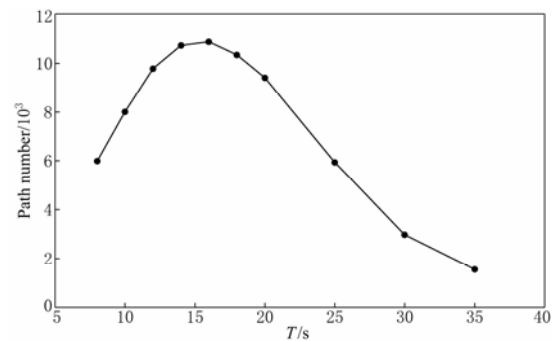

Figure 3 Number of selected phase velocity measurements as a function of period (T).

microseismic band, and then decreases with period so that at 35 s there are only about 1 500 measurements.

3 Phase velocity measurements and tomography

We measure phase velocity dispersion curves by automatic frequency-time analysis (FTAN). As shown by Bensen et al. (2007), phase velocity measurements are much more accurate and possess smaller uncertainties than group velocity measurements. Phase velocity is measured from instantaneous phase by considering the phase ambiguity. We follow Lin et al. (2008) to resolve the 2π phase ambiguity by tracing phase velocity dispersion curves from long periods to short periods, because we have reliable reference dispersion curves at long periods from earthquake surface wave tomography (e.g., Shapiro et al., 2002).

Figure 4 shows two examples of cross correlations and the corresponding phase velocity dispersion curves. The path between stations AXI and YUB lies mostly within the Sichuan basin, and the path between stations MEK and JLO is within southeastern Tibet. Phase velocities at short periods (<12 s) in the Sichuan basin are significantly lower than in southeastern Tibet because there is a thick sedimentary layer in the Sichuan basin. However, at periods longer than 12 s, phase velocities in the Sichuan basin are significantly higher than in southeastern Tibet, indicating that the velocity of the crust within the Sichuan basin is faster than within the Tibetan plateau.
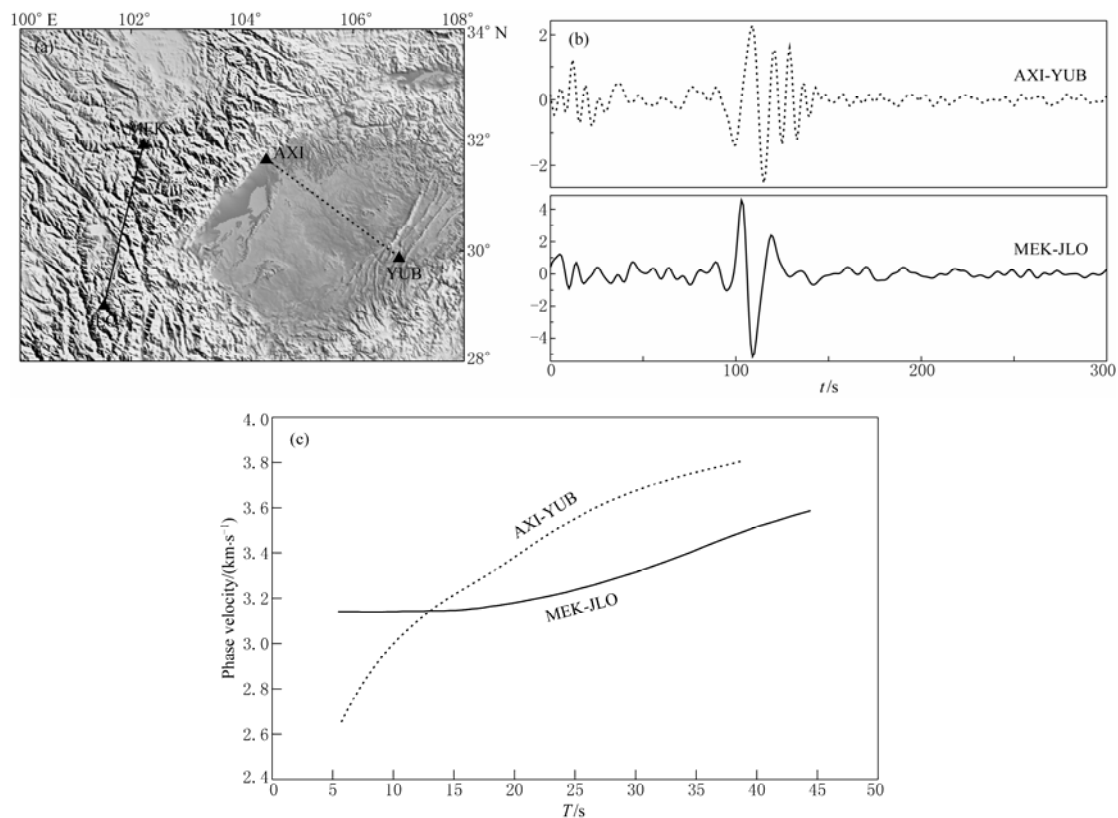

Figure 4   (a) Ray paths between stations AXI and YUB and between stations MEK and JLO; (b) 5−35 s band-pass filtered symmetric-component cross-correlations for the station pairs AXI-YUB and MEK-JLO; (c) The measured Rayleigh wave phase velocity dispersion curves based on the cross-correlations shown in (b).

Rayleigh wave phase dispersion measurements are used to invert for phase velocity maps on a 1 ×1 spatial grid using the tomographic method of Barmin et al. (2001), which also provides resolution information (Levshin et al., 2005). This method is based on minimizing a penalty function composed of a linear combination of data misfit, model smoothness, and the perturbation to a reference model for isotropic wave velocity. Each row of the resolution matrix is a resolution surface (or kernel) for a specific grid node. We summarize the

information of the resolution surface at each spatial node by fitting a 2-D symmetric spatial Gaussian function to the resolution surface at each node: $A\exp(-|r|^2/2\gamma^2)$, here A is the amplitude of the fit-Gaussian at the target node, and r is the location of the target node. The spatial resolution at each node is defined as twice the standard deviation of this Gaussian function γ. Examples of resolution maps and associated path coverage are plotted in Figure 5 for the 16 s and 30 s period measurements. Resolution is estimated to be about 100 km in this study region.
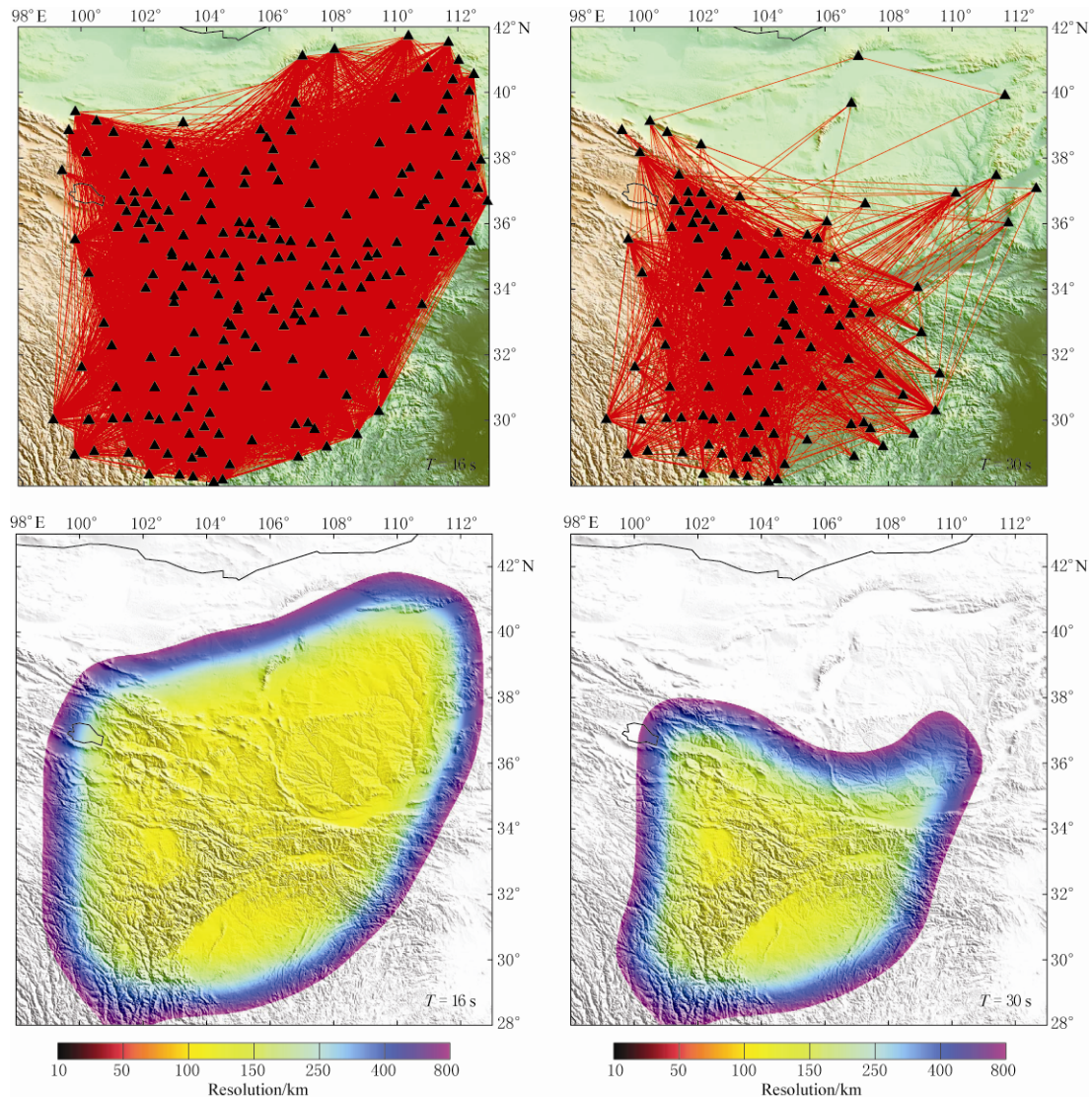

Figure 5   Ray path coverages (top) and resolution maps (bottom) at periods (T) of 16 and 30 s. Resolution is presented in units of km and is defined as twice the standard deviation of a 2-D Gaussian fit to the resolution surface at each geographic node (e.g., Barmin et al., 2001).

4 Phase velocity maps

Selected phase velocity maps at periods of 8, 12, 18, 25, 30 and 35 s are plotted in Figure 6 as perturbations relative to the average values at each individual period: 3.07, 3.15, 3.27, 3.42, 3.51 and 3.60 km/s, respectively.

The features of the phase velocity maps vary gradually with period due to the overlap of the Rayleigh wave depth-sensitivity kernels. The depth of maximum phase velocity sensitivity of Rayleigh waves to shear velocity is about one-third of a wavelength. Shear velocity sensitivity kernels of Rayleigh phase velocities are plotted to
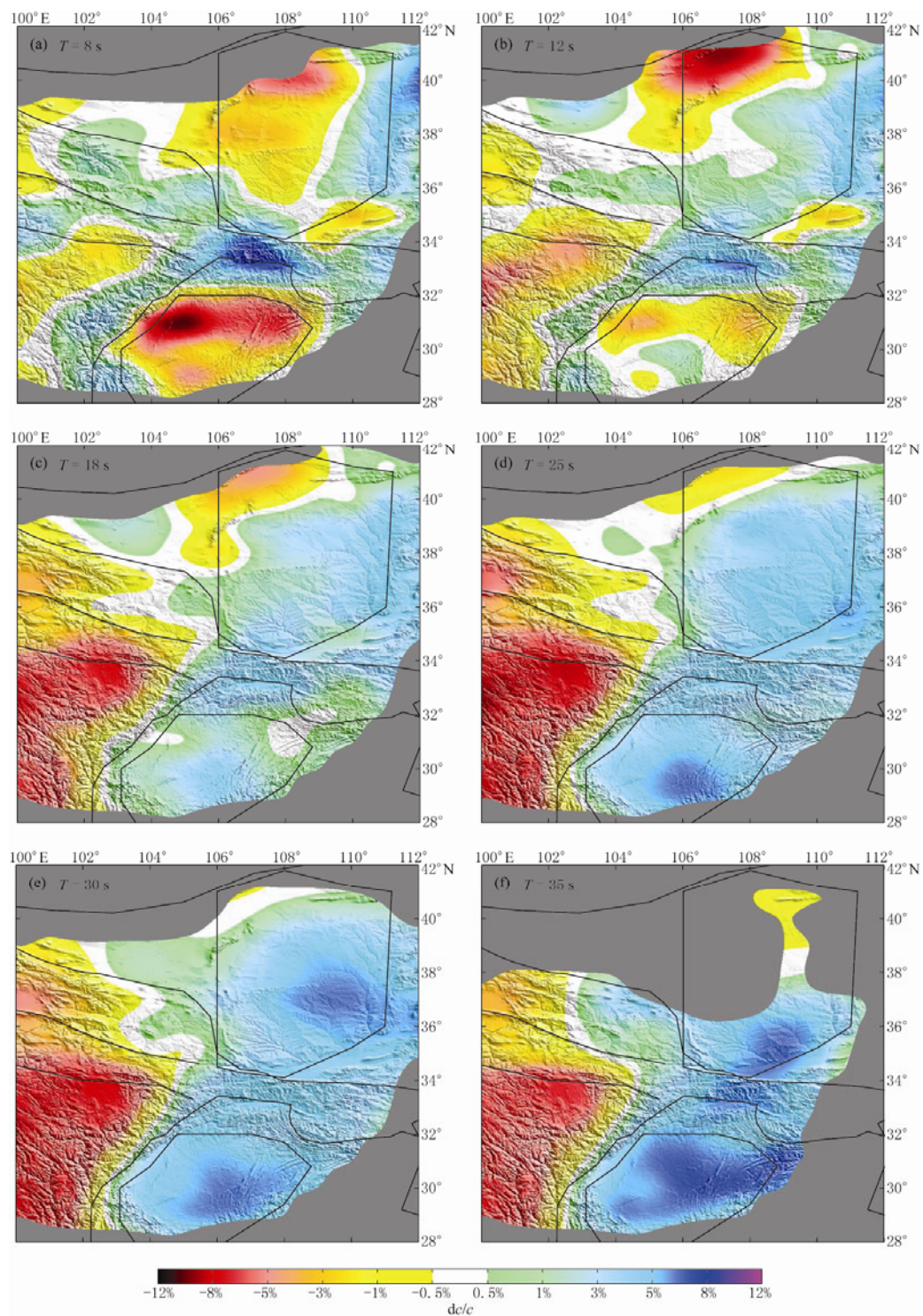
Figure 6 Phase velocity maps at periods of 8 (a), 12 (b), 18 (c), 25 (d), 30 (e) and 35 s (f). Phase velocities are plotted as perturbations relative to the average value at each period. The black lines outline the boundaries of different blocks. dc/c is the perturbation of the phase velocity.

guide the interpretation (Figure 7). The 1D v_S model used to construct the kernels is taken at (101.0 E, 32.0 N) from the 3D model of Shapiro and Ritzwoller (2002). In the short period band (6−14 s), the phase velocities are
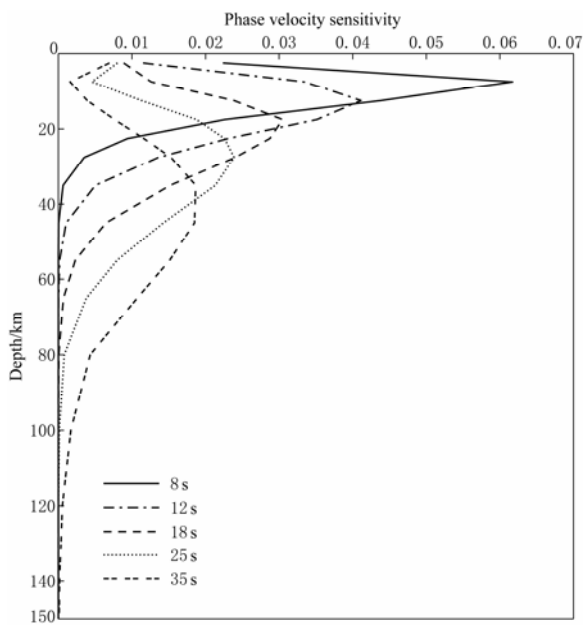
Figure 7 Shear velocity sensitivity kernels of Rayleigh phase velocities at periods of 8, 12, 18, 25 and 35 s.

dominantly sensitive to shear wave velocities in the shallow crust. As the shear wave velocities of sediments (1–2 km/s) are much lower than those of crystalline rocks, the phase velocity anomalies at the short periods depict the distributions of the sedimentary basins. The 8 and 12 s phase maps shown in Figures 6a and 6b exhibit low phase velocity zones in the northwestern Ordos block, the Sichuan basin and the Weihe graben. Compared with the 8 s map, the amplitudes of the low velocity anomalies on the 12 and 18 s phase maps in the Sichuan basin decrease quickly with period. At 18 s, the low velocity anomaly is replaced by a slightly high velocity anomaly (Figure 6c); while in the northwestern part of the Ordos block, the low phase velocity anomaly remains strong in the 12 and 18 s phase maps. Even in the 25 s phase speed map (Figure 6d), this low velocity area in the northwestern Ordos block remains. This implies that the sedimentary layer in the northwestern part of the Ordos block is considerably thicker than that in the Sichuan basin. There are also significant velocity variations at short periods within the Sichuan basin and the Ordos block. Within the Ordos block, low velocity anomalies at short periods in the northwest are much stronger than those in other areas within the block, which means that the sedimentary layer in the northwestern Ordos block is much thicker than in other parts. Within the Sichuan basin, the strongest low velocity anomalies at short periods are present in the northern

part of the basin, which may imply that sedimentary layers in the Sichuan basin are thicker in the northern part than in the central and the southern parts.

At short periods (<20 s), the northeastern Tibetan plateau is dominated by low phase velocities, which indicates the crust in the eastern part of the Tibetan plateau may be warmer and perhaps weaker than surrounding non-basin regions. The lower velocity in the Tibetan plateau persists at intermediate and long periods (>25 s), which may be due to two main reasons. The first is very thick crust in the Tibetan plateau (>65 km) and the other is that the temperature of the lower crust is probably higher than in surrounding areas, such as the Sichuan basin and the Ordos block.

At long periods (>25 s), Rayleigh waves become primarily sensitive to crustal thickness and the shear velocities in the lower crust and uppermost mantle (Figure 7). The phase velocity anomalies at periods from 25 s to 35 s vary approximately inversely with crustal thickness, with high velocities in regions with thin crust and low velocities in regions with thick crust (Figures 6d–6f). Very high velocity anomalies at 25–35 s periods are centered on the Ordos block and the Sichuan basin, especially pronounced at 35 s period (Figure 6f).

5 Shear wave velocity structure

More detailed interpretation requires that the phase velocity maps from ambient noise tomography at periods from 6 s to 35 s be used to invert for shear wave velocities in the crust and uppermost mantle. Rayleigh wave phase velocities primarily depend on S-wave, less on P-wave, velocities and density. Thus, in the inversion, we fix the densities using the AK135 density model and only estimate S-wave velocity by scaling P-wave velocity to S-wave velocity assuming the materials are Poisson solids. The relation between shear-wave speeds and phase velocities is non-linear. We linearize the relation and iterate until convergence using Saito's algorithm (Saito, 1988) to compute the synthetic phase velocities and partial derivatives with respect to changes in P-wave and S-wave speeds. Depth-dependent shear wave speeds are parameterized in eleven constant v_S layers from the Earth's surface to 100 km depth with 5 km layer thickness in the top two layers and 10 km layer thickness in the remaining layers. Because of the nonlinearity and also the limitations of surface wave vertical resolution, the model parameters are weakly damped by assigning prior standard deviations to the diagonal terms of the model covariance matrix and are

also smoothed by adding terms to the first off-diagonal. The goal of this inversion is to produce a model that is vertically smooth but also is free to vary significantly from the starting model. We obtain starting models in our study region from the global model of Shapiro et al. (2002). We have also tried the inversion with different initial models and have found that their effect on the final v_S is quite small.

The v_S maps in different depths are shown in Figure 8. In these maps some areas with low resolution are clipped based on the resolution maps which are shown in Figure 6. In order to analyze the detail shear wave
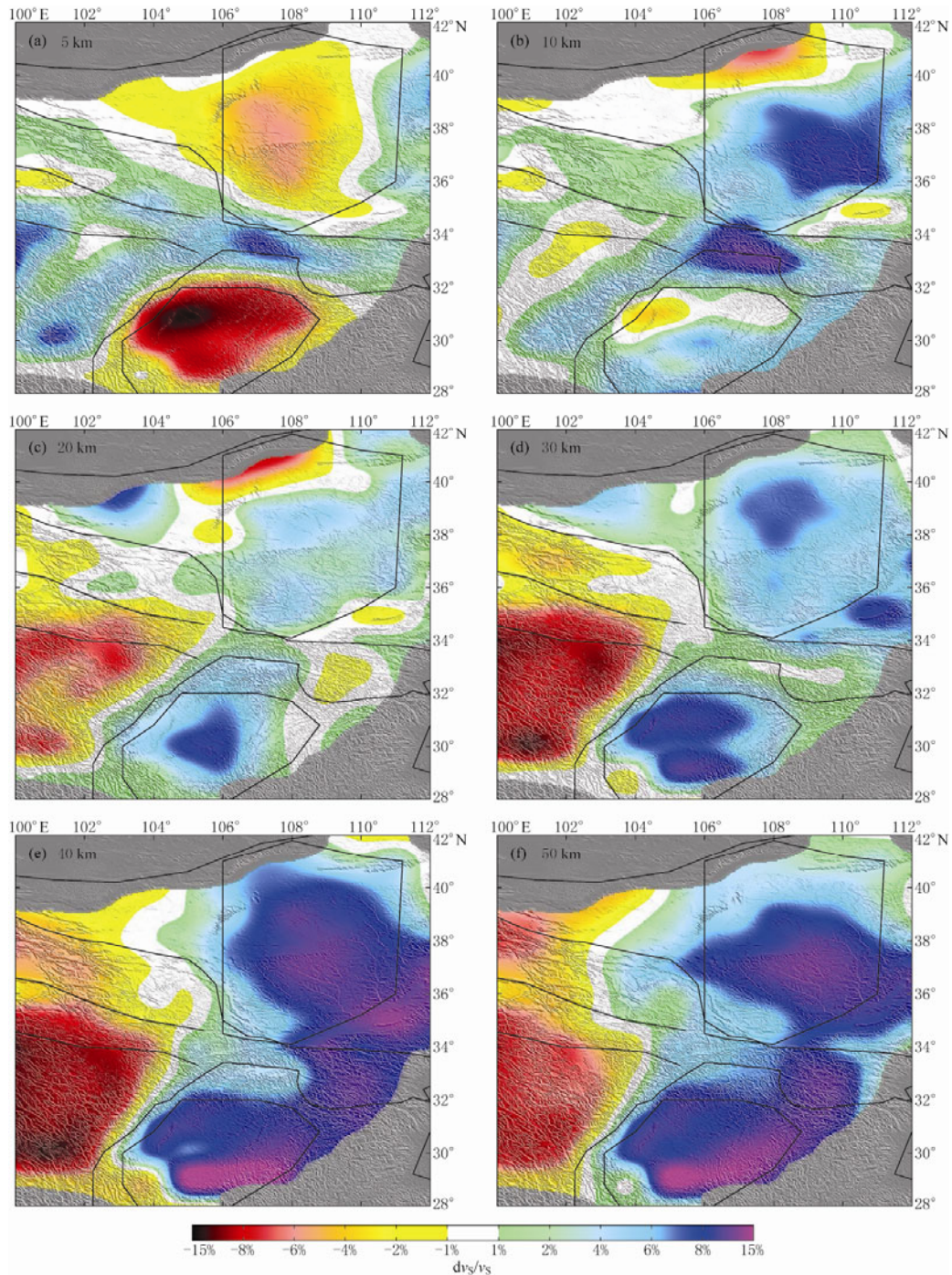

Figure 8 Velocity maps at depths of 5 (a), 10 (b), 20 (c), 30 (d), 40 (e), and 50 km (f) respectively. Shear wave velocity are plotted as perturbations relative to the average value at each depth.

structure in horizontal and vertical directions, we select ten profiles along latitudinal direction and ten profiles along longitudinal direction. The locations of vertical v_S profiles are shown in Figure 9 and the profiles themselves appear in Figures 10 and 11. The profiles align either in longitudes along 101 E to 110 E or latitudes along 31 N to 40 N with an interval of 1 degree. The shear wave velocity profiles in the longitudinal direction are plotted in Figure 10 and those in the latitudinal directions in Figure 11. The areas with low resolution are also clipped based on the resolution maps.
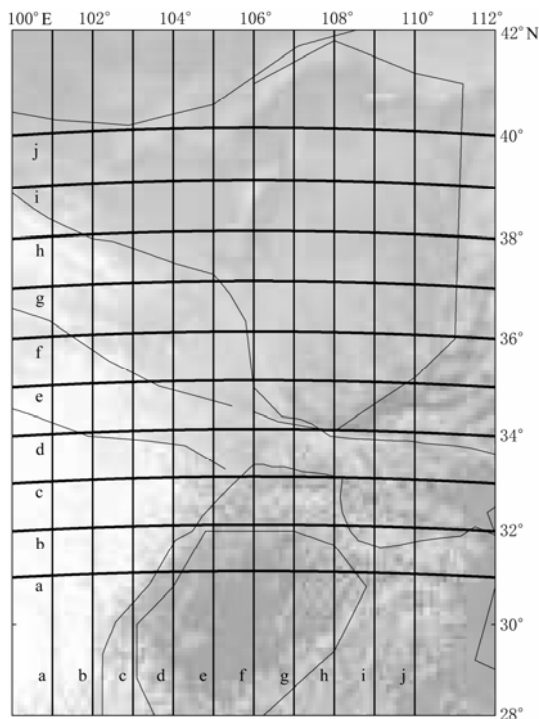

Figure 9 Locations of twenty v_S profiles along longitudinal direction and latitudinal direction shown in Figures 10 and 11. The intervals of the profiles are one degree both in two directions.

Comparing the four profiles from 101 E to 104 E plotted along longitudes (Figure 10a−10d), a low shear wave velocity zone appears in the northeastern Tibetan plateau. The latitude range of the low velocity zone at 101 E is from 30 N to 35 N. From west to east, the width of the low velocity zone narrows. In Figure 10d (104 E), the low velocity zone can only be observed from 33 N to 35 N, and its maximum depth also decreases from 45 km to 35 km. On the cross section at 105 E (Figure 10e), the size of this low velocity zone reduces and the shear wave velocity returns to close to

the average. Further east (Figure 10f−10h), this low velocity zone disappears entirely.

It is commonly hypothesized that lithospheric materials flow out of the Tibetan plateau towards the east mainly along two channels: one is along the northeastern gateway of the Tibetan plateau and the other one is along the southeastern gateway (e.g., Molnar and Tapponnier, 1975; Tapponnier and Molnar, 1977). A low velocity zone is observed in the southeastern gateway (Yao et al., 2008). As expected from the flow model, low velocity anomalies should also be present in the northeastern part of the Tibetan plateau and along the path where mass is expected to flow. However, based on our v_S model, the low velocities appear to be limited to the northeast end of the Tibetan plateau. There is no obvious low velocity channel beyond the boundary towards the convergence area (the Qinling orogen) between the Ordos block and the Sichuan basin (Figures 10e−10h and Figures 11b, 11c). Thus, material may flow out of the Tibetan plateau northeastward and reach the northeastern edge of the plateau at the current stage, but does not flow through the channel between the Ordos block and the Sichuan basin in the crust and uppermost mantle. Probably in the asthenosphere or deeper part, there is a low velocity zone which provides possible channel for the eastward flow.

From 108 E to 110 E (Figures 10h−10j), where the longitudinal profiles pass through the Weihe graben, a weak low velocity belt is observed beneath the Weihe graben that is coincident with the low topography of the graben. The profiles in the latitudinal direction clearly show large variations of Moho depth across different tectonic blocks. The crustal thickness decreases from about 65 km in the middle part of the Tibetan plateau to about 50 km in the eastern margin of the Tibetan. Across the Longmenshan orogen, the crustal thickness quickly decreases to about 40 km (Figures 11a, 11b), resulting in a sharp boundary between the Tibetan plateau and the Sichuan basin. Except for the sedimentary layers at the surface, the crust and uppermost mantle beneath the Sichuan basin and most of the Ordos block exhibit high shear wave velocities, which indicates that the interior structures of both the Sichuan basin and the Ordos block are strong. In the northern part of the Ordos block, a low shear wave velocity anomaly is seen in the upper and the middle crust (Figure 11j), which may imply that the northern margin of the Ordos block is relatively weak and may explain why the Hetao graben has developed.
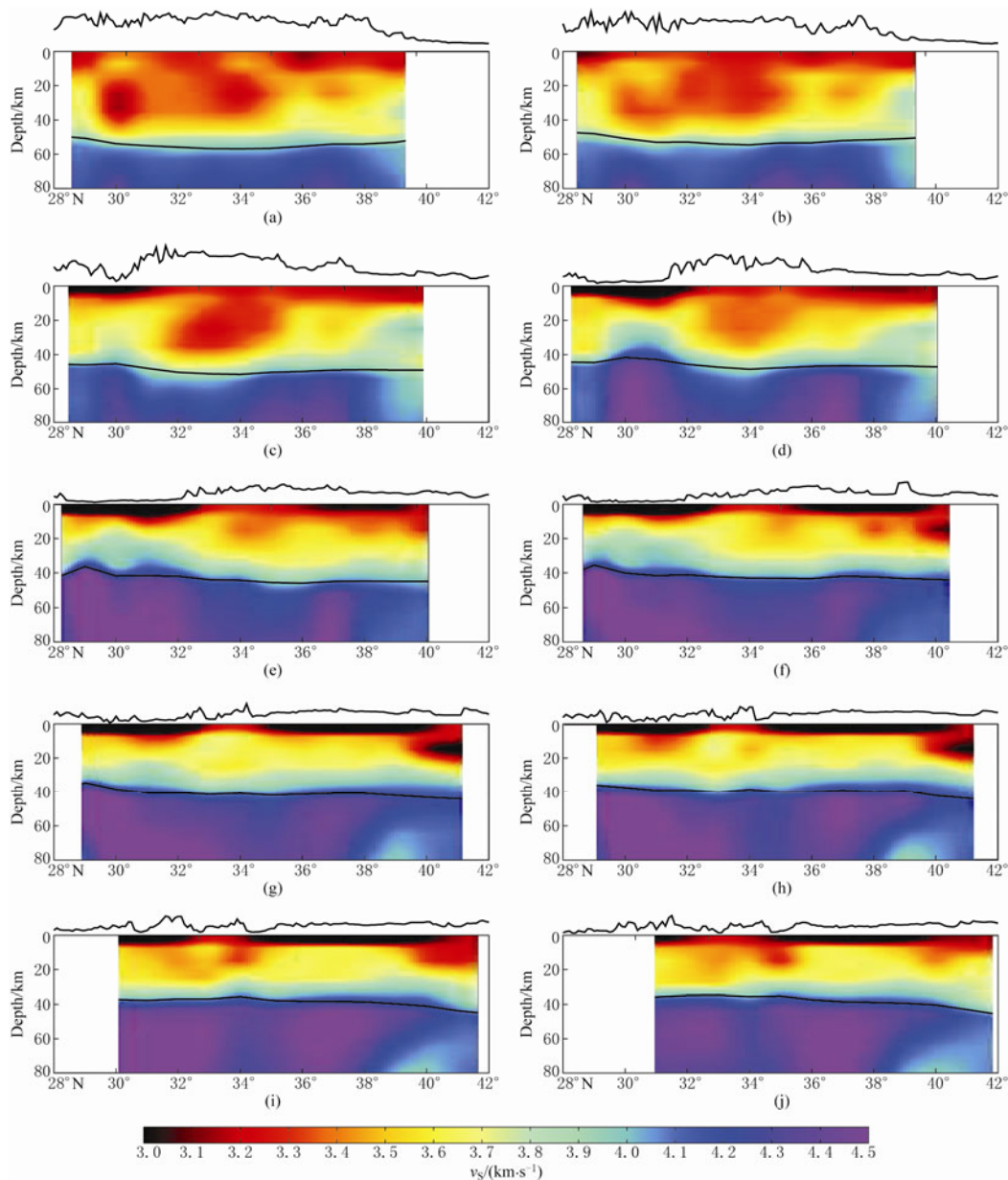
Figure 10   Vertical shear wave velocities along longitudes. The locations of the profiles are delineated by the thin lines in Figure 9. From the subplots (a) to (j), the correspondent longitude is from 101 E to 110 E.

6 Summary

We apply ambient noise tomography to significant data resources available in a region including the northeastern Tibetan plateau, the Ordos block and the Sichuan basin. The seismic stations come from the Chinese provincial networks in Shaanxi, Sichuan, Gansu, Shanxi provinces and Inner Mongolia autonomous region with the number of stations totaling about 160. Ambient noise cross-correlations are performed on data from these networks obtained from 2007 to 2009. Inter-station Rayleigh phase dispersion curves at 6–35 s period are measured from cross-correlations of vertical components and are then used to invert for Rayleigh phase velocity maps.

The resulting phase velocity maps have resolutions between 100 km and 150 km across most of the studied area and reveal a wealth of velocity features associated with tectonic structures. Rayleigh phase velocity maps at short periods show strong low velocity anomalies
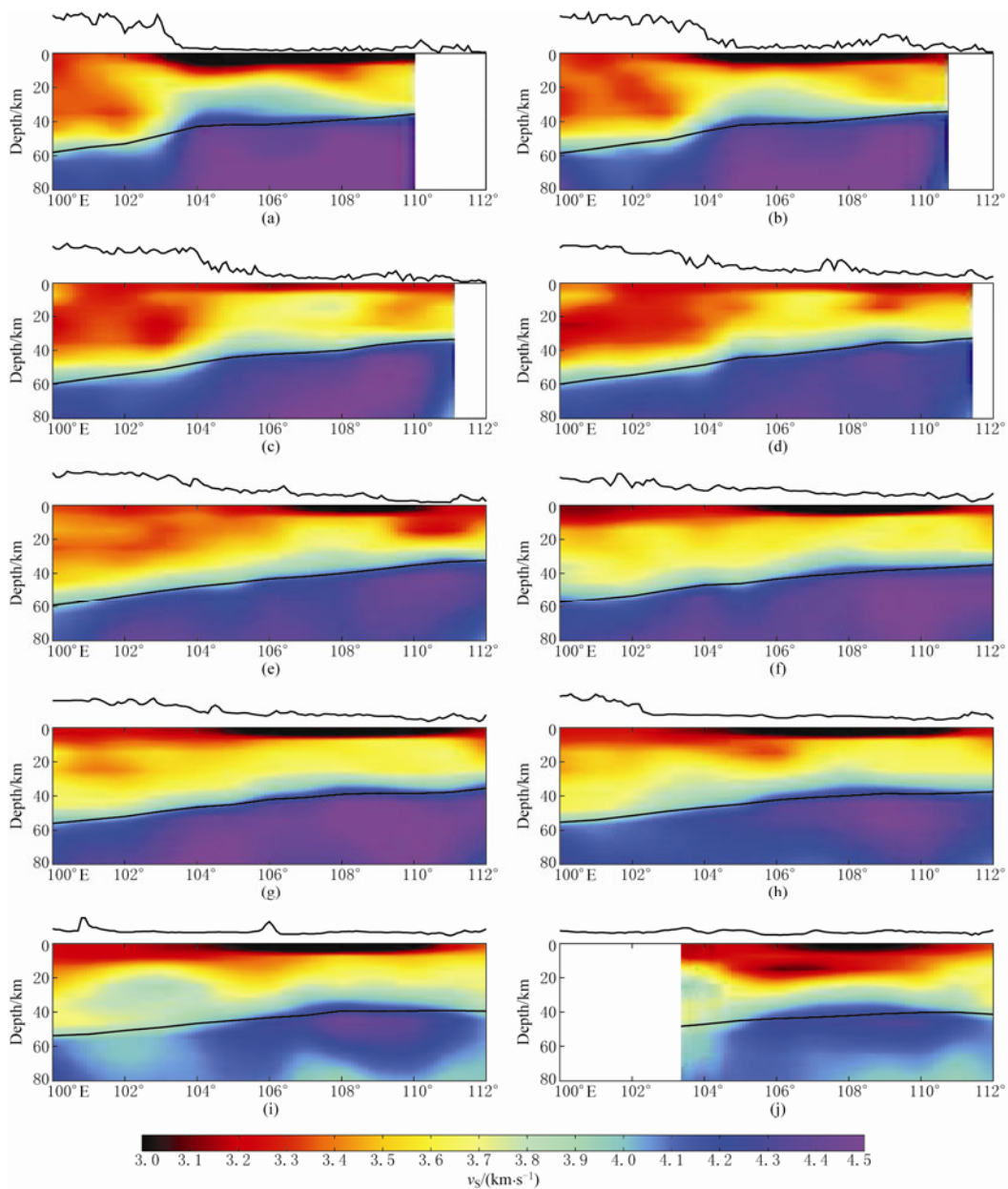
Figure 11 Vertical shear wave velocity along latitudes. The locations of the profiles are delineated by the thick lines in Figure 9. From subplots (a) to (j), the correspondent latitude is from 31 N to 40 N.

correlated with the major sedimentary deposits of the Sichuan basin, the northwestern part of the Ordos and the Weihe graben. At intermediate and long periods (>25 s), strong high velocity anomalies are observed within the Ordos block and the Sichuan basin. Phase velocities in the northeastern Tibetan plateau at all periods are overall lower than in the surrounding regions. There is no low phase velocity zone at the boundary (the Qinling orogen) between the Ordos block and the Sichuan basin.

Shear wave velocities in the crust and uppermost mantle show strong variations between the Tibetan plateau, the Sichuan basin and the Ordos block. Both the Ordos block and the Sichuan basin are dominated by high shear wave velocities in the crust and uppermost mantle. There is a triangle-shaped low velocity zone located in the northeastern Tibetan plateau, with the width of the triangle narrowing towards the eastern margin of the plateau. There is no apparent low velocity

zone in the Qinling orogen crust, suggesting that material in the crustal and the uppermost mantle may not be able to flow eastward through the boundary between the Ordos block and the Sichuan basin.

References

Barmin M P, Ritzwoller M H and Levshin A L (2001). A fast and reliable method for surface wave tomography. *Pure Appl Geophys* **158**: 1 351–1 375.

Bendick R and Flesch L (2007). Reconciling lithospheric deformation and lower crustal flow beneath central Tibet. *Geology* **35**: 895–898, doi:10.1130/G23714A.1.

Bensen G D, Ritzwoller M H and Shapiro N M (2008). Broadband ambient noise surface wave tomography across the United States. *J Geophys Res* **113**: B05306, doi:10.1029/2007JB005248.

Bensen G D, Ritzwoller M H, Barmin M P, Levshin A L, Lin F, Moschetti M P, Shapiro N M and Yang Y (2007). Processing seismic ambient noise data to obtain reliable broad-band surface wave dispersion measurements. *Geophys J Int* **169**: 1 239–1 260.

Burchfiel B C, Royden L H, van der Hilst R D, Hager B, Chen Z-L, King R, Li C, Lu J-N, Yao H-J and Kirby E (2008). A geological and geophysical context for the Wenchuan earthquake of 12 May 2008, Sichuan, People's Republic of China. *GSA Today* **18**(7): 4–11, doi:10.1130/GSATG18A.1.

Clark M K, Bush J and Royden L (2005). Dynamic topography produced by lower crustal flow against rheological strength heterogeneities bordering the Tibetan plateau. *Geophys J Int* **162**: 575–590.

Huang Z-C, Xu M-J, Wang L-S, Mi N, Yu D-Y and Li H (2008). Shear wave splitting in the southern margin of the Ordos block, north China. *Geophys Res Lett* **35**: L19301, doi:10.1029/2008GL035188.

Levshin A L, Barmin M P, Ritzwoller M H and Trampert J (2005). Minor-arc and major-arc global surface wave diffraction tomography. *Phys Earth Planet Inter* **149**: 205–223.

Liang C-T and Song X-D (2006). A low velocity belt beneath northern and eastern Tibetan plateau from Pn tomography. *Geophys Res Lett* **33**: L22306, doi:10.1029/2006GL027926.

Lin F, Moschetti M P and Ritzwoller M H (2008). Surface wave tomography of the western United States from ambient seismic noise: Rayleigh and Love wave phase velocity maps. *Geophys J Int* **173**(1): 281–298, doi:10.1111/j1365-246X.2008.03720.x.

Molnar P and Tapponnier P (1975). Cenozoic tectonics of Asia: effects of a continental collision. *Science* **189**: 419–426.

Moschetti M P, Ritzwoller M H and Shapiro N M (2007). Surface wave tomography of the western United States from ambient seismic noise: Rayleigh wave group velocity maps. *Geochem Geophys Geosys* **8**: Q08010, doi:10.1029/2007GC001655.

Royden L H, Burchfiel B C and van der Hilst R D (2008). The geological evolution of the Tibetan plateau. *Science* **321**: 1 054–1 058.

Royden L H, Burchfiel B C, King R W, Wang E, Chen Z L, Shen F and Liu Y P (1997). Surface deformation and lower crustal flow in eastern Tibet. *Science* **276**: 788–790.

Saito M (1988). DISPER80: a subroutine package for the calculation of seismic normal-mode solutions. In: Doornbos D J ed. *Seismological Algorithms*. Elsevier, New York, 293–319.

Shapiro N M and Ritzwoller M H (2002). Monte-Carlo inversion for a global shear velocity model of the crust and upper mantle. *Geophys J Int* **151**: 88–105.

Shapiro N M, Campillo M, Stehly L and Ritzwoller M H (2005). High resolution surface wave tomography from ambient seismic noise. *Science* **307**(5715): 1 615–1 618.

Tapponnier P and Molnar P (1977). Active faulting and tectonics in China. *J Geophys Res* **82**: 2 905–2 930.

Yang Y, Ritzwoller M H, Lin F C, Moschetti M P and Shapiro N M (2008). The structure of the crust and uppermost mantle beneath the western US revealed by ambient noise and earthquake tomography. *J Geophys Res* **113**: B12310.

Yao H, Beghein C and van der Hilst R D (2008). Surface-wave array tomography in SE Tibet from ambient seismic noise and two-station analysis: II — Crustal and upper mantle structure. *Geophys J Int* **173**(1): 205–219, doi:10.1111/j.1365-246X.2007.03696.x.

Zhang Y Q, Mercier J L and Vergely P (1998). Extension in the graben systems around the Ordos (China), and its contribution to the extrusion tectonics of south China with respect to Gobi-Mongolia. *Tectonophysics* **285**: 41–75, doi:10.1016/S0040-1951(97)00170-4.